Disentangling lattice and electronic contributions to the metal–insulator transition from bulk vs. layer confined $RNiO_3$

Alexandru B. Georgescu[a,1], Oleg E. Peil[b], Ankit S. Disa[c], Antoine Georges[a,d,e,f], and Andrew J. Millis[a,g]

[a]Center for Computational Quantum Physics, Flatiron Institute, New York, NY 10010; [b]Group of Computational Materials Design, Materials Center Leoben, 8700 Leoben, Austria; [c]Condensed Matter Department, Max Planck Institute for the Structure and Dynamics of Matter, 22761 Hamburg, Germany; [d]Institut de Physique, Collège de France, 75005 Paris, France; [e]Centre de Physique Théorique Ecole Polytechnique, CNRS, Universite Paris-Saclay, 91128 Palaiseau, France; [f]Department of Quantum Matter Physics, University of Geneva, 1211 Geneva 4, Switzerland; and [g]Department of Physics, Columbia University, New York, NY 10027

Edited by Robert J. Cava, Princeton University, Princeton, NJ, and approved June 12, 2019 (received for review November 5, 2018)

In complex oxide materials, changes in electronic properties are often associated with changes in crystal structure, raising the question of the relative roles of the electronic and lattice effects in driving the metal–insulator transition. This paper presents a combined theoretical and experimental analysis of the dependence of the metal–insulator transition of $NdNiO_3$ on crystal structure, specifically comparing properties of bulk materials to 1- and 2-layer samples of $NdNiO_3$ grown between multiple electronically inert $NdAlO_3$ counterlayers in a superlattice. The comparison amplifies and validates a theoretical approach developed in previous papers and disentangles the electronic and lattice contributions, through an independent variation of each. In bulk $NdNiO_3$, the correlations are not strong enough to drive a metal–insulator transition by themselves: A lattice distortion is required. Ultrathin films exhibit 2 additional electronic effects and 1 lattice-related effect. The electronic effects are quantum confinement, leading to dimensional reduction of the electronic Hamiltonian and an increase in electronic bandwidth due to counterlayer-induced bond-angle changes. We find that the confinement effect is much more important. The lattice effect is an increase in stiffness due to the cost of propagation of the lattice disproportionation into the confining material.

transition metal oxide | metal–insulator transition | heterostructure | epitaxial constraint | layer confinement

Metal–insulator transitions (MITs) in correlated electron materials typically involve changes in both the electronic and atomic structures. The relative importance of the 2 effects has been the subject of extensive discussion (1–8). In this paper, using a recently developed theoretical approach (3, 8), we argue that comparison of few-layer and bulk materials yields considerable insight into the relative importance of electronic and lattice contributions, essentially because these are affected by heterostructuring in opposite ways. We disentangle these effects by independently changing each. Motivated by recent experimental (9–25) and theoretical (8, 13, 26–36) results, we focus here on the rare-earth nickelate family of materials. The concepts, formalism, and findings are applicable to wide classes of materials.

The rare-earth nickelates have chemical formula $RNiO_3$ (R is a rare-earth metal of the lanthanide rare-earth series). In bulk, at high T, they are metallic and form an orthorhombic Pbnm structure (except for R = La, for which the structure is rhombohedral) that is a distorted ABO_3 cubic perovskite in which the Ni ions are equivalent up to a rotation and translation. For all R, except for La, the bulk materials undergo an MIT, as T is decreased. The transition is first-order, and the low-T phase has a $P2_1/n$ structure with 2 fundamentally inequivalent Ni sites characterized by an electronic charge disproportionation ΔN and a lattice distortion Q, both defined more precisely below. The relative roles of the 2 have been the subject of debate. The issue has typically been addressed by calculations (typically performed at fixed crystal structure) and experiments on a specific material or on members of a family of materials and has not been resolved. Similar issues arise in many other transition metal oxide materials.

Recent experiments (9) report that in $NdNiO_3/NdAlO_3$ (NNO/NAO) superlattices in which 1 or 2 monolayers of NNO are separated by many layers of the wide-gap insulator NAO, the MIT occurs at a much higher temperature than in the bulk, while the X-ray signatures of the lattice distortion are much less pronounced in the superlattices than in bulk. These experiments suggest that heterostructuring affects electronic and lattice properties differently and, thus, that a comparative examination of the 2 material forms can help disentangle the relative importance of electronic and lattice contributions to the MIT. In this paper, we theoretically investigate the differences between bulk NNO and superlattice NNO/NAO materials using a theoretical approach previously applied to bulk nickelates (5, 8, 27, 29, 31–33, 37–39) and to ruthenates (3).

In Fig. 1, we represent the main phenomenology that we disentangle in this paper, as exemplified on the bilayer NNO. Namely, the structural distortions in the material become inhomogenous due to the presence of the NAO counterlayer and the absence of a driving force on the interfacial oxygen from the aluminum

Significance

Our combined theoretical and experimental study of bulk and heterostructured forms of a correlated electron material leads to insights into the metal–insulator transition. Comparison of single-layer, bilayer, and very thick samples validates a combined ab-initio/many-body theoretical approach and enables a clear disentangling of electronic and lattice contributions to the transition by independently changing each. Analysis of the lattice relaxations associated with the metal–insulator transition highlights the importance of the elastic properties of and propagation of distortions into the electronically inert counterlayer, defining a control parameter for tuning electronic properties. Counterlayer-induced bond-angle changes and electronic confinement provide separate tuning parameters, with bond-angle changes found to be a much less effective tuning parameter.

Author contributions: A.B.G., O.E.P., A.G., and A.J.M. designed research; A.B.G. and A.S.D. performed research; A.B.G. analyzed data; and A.B.G. wrote the paper.

The authors declare no conflict of interest.

This article is a PNAS Direct Submission.

[1]To whom correspondence may be addressed. Email: ageorgescu@flatironinstitute.org.

This article contains supporting information online at www.pnas.org/lookup/suppl/doi:10.1073/pnas.1818728116/-/DCSupplemental.

Published online July 2, 2019.

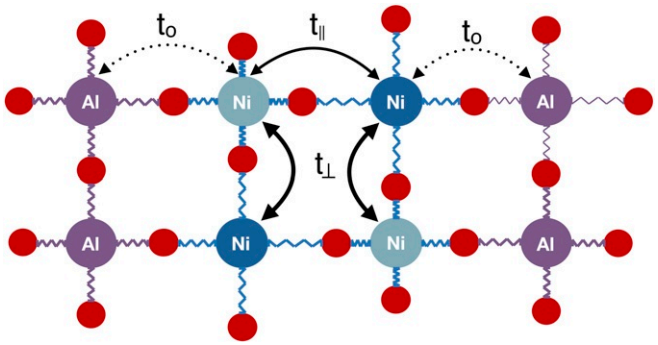

Fig. 1. Heterostructuring $NdNiO_3$ (NNO) with $NdAlO_3$ (NAO): Structural distortions are represented as motion (not to scale) of oxygen ions (red circles) away from the center of Ni–Ni and Ni–Al bonds; note that the distortions do not propagate significantly into the Al layers, and are of reduced amplitudes along the Ni–Al bonds. The different colors of the Ni atoms represent the electronic disproportionation. The kinetic energy of the Ni e_g electrons is reduced by confinement, as electrons are not allowed to hop through the insulating NAO layers ($|t_0| \ll |t_\perp|, |t_\parallel|$), while $|t_\parallel| < |t_\perp|$ due to propagation of bond angles from NAO.

atom. In our effective model, this leads to an increased effective stiffness of the bond disproportionation mode, as the same force from the nickel atoms leads to a lower average oxygen displacement. On the electronic structure, the layer confinement of the material leads to suppressed hopping along the z direction, while the propagation of bond angles from NAO to NNO leads to a small increase of the Ni–Ni hopping in-plane compared with the out-of-plane Ni–Ni hopping in the bilayer.

Energy

Central to our discussion is an expression for the energy difference ΔE between the insulating and metallic phases as a function of lattice distortion Q and charge disproportionation ΔN (3, 8):

$$\Delta E(Q, \Delta N) = \frac{kQ^2}{2} - \frac{1}{2} gQ\Delta N + E_{el}(\Delta N). \quad [1]$$

The first term is the elastic energy cost of establishing the lattice distortion, the middle term is the leading symmetry allowed coupling between the structural- and electronic-order parameters, and the final term is the energy associated with the electronic transition. The 3 control parameters are thus k, g, and the combination of interaction parameters and bandwidths that determines $E_{el}(\Delta N)$. This energy formalism is general and can be applied in the context of density functional theory (DFT), DFT+U (where U stands for Hubbard U), DFT+ dynamical mean field theory (DMFT), and other formalisms. As the first term is meant to include all but the contribution of the correlated electrons, the value of k is independent of formalism and can be obtained by interpolation from multiple structures with varying Q from DFT alone. The lattice distortion Q leads to an on-site (Peierls) potential difference between the 2 inequivalent sites $\Delta_S = gQ$ (33), which is defined as the difference between the average of the on-site energies of the extended e_g orbitals. This defines the second term in the energy formalism, characterized by a coupling between the electronic and lattice degrees of freedom. Finally, $E_{el}(\Delta N)$ is the energy of the correlated electrons alone and depends explicitly on the approach we use to solve the correlated problem.

To quantify the lattice distortion Q, we define the average bond disproportionation between 2 octahedra:

$$Q = \sqrt{\frac{\sum_i \left(l_{LB}^{(i)} - l_{SB}^{(i)}\right)^2}{6}}, \quad [2]$$

where $l^{(i)}$ are the lengths of the Ni–O bonds, and LB and SB correspond to the long-bond and short-bond octahedra, respectively. Within our DFT+DMFT formalism, we define the electronic disproportionation ΔN as:

$$\Delta N = N_{HF} - N_{LF}, \quad [3]$$

with HF = higher filling and LF = lower filling. These densities are the occupancies of the e_g antibonding orbitals in our low-energy model and are simply obtained as the trace of the local density matrix on each site. When there is structural disproportionation, HF corresponds to LB, and LF corresponds to SB. The occupancy of the 2 sites is defined within a model describing the Wannier low-energy antibonding e_g bands as defined in *SI Appendix*.

A more detailed description of the process by which we fix and determine the control parameters is given in *SI Appendix*; here, we summarize the findings and give physical interpretations.

In a previous work on bulk perovskites, the structural stiffness parameter k was found to vary only slightly as the rare-earth ion was changed (8). We find that heterostructuring has a stronger effect, with k increasing from k = 15.86 eV/Å^2 for bulk NNO, to 17.71 eV/Å^2 for the bilayer structure and 20.18 eV/Å^2 for the monolayer. The fundamental difference between bulk and layered systems appears at the interface between the 2 components of the heterostructure. A schematic of the bond-disproportionation mode in the bilayer as obtained from DFT+U structural relaxations is shown in Fig. 2. The essential point is that the lattice distortion propagates a short distance into the counterlayer, and the stiffness to this intertwined layer–counterlayer distortion is larger than for the nickelate material alone.

We represent the bond-disproportionation mode and its propagation in Fig. 2 for a particular Q for the bilayer. This structure is obtained through a DFT+U relaxation of a $(NNO)_2/(NAO)_2$ heterostructure, using a U = 4 eV and a $c(2 \times 2)$ unit cell in the xy plane, imposing ferromagnetic order on the system. This results in 2 pairs of inequivalent NiO_6 octahedra. The average bond disproportionation Q for this relaxed structure is Q = 0.078 Å. This is slightly smaller than the bond disproportionation obtained from a relaxation within DFT+U with U = 4 eV for a bulk 20-atom unit cell, for which we obtain Q = 0.081 Å, and smaller than the disproportionation Q = 0.087 Å similarly obtained for the monolayer. Further details on the calculations and structures and the estimates of the displacements along the Ni–Ni and Ni–Al directions, as pictured in Fig. 2, can be found in *SI Appendix*.

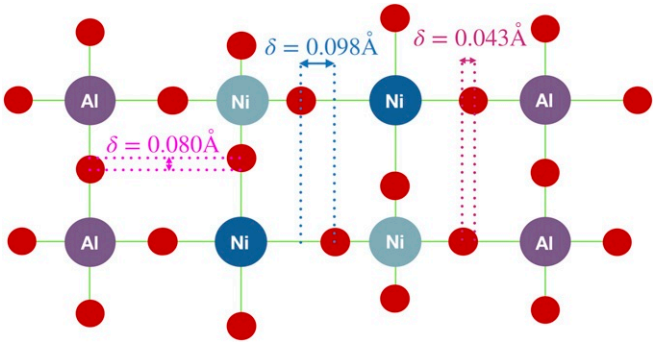

Fig. 2. Schematic of the bond-disproportionation modes in the NNO bilayer (NNO_2/NAO_2) and its propagation into nearby NAO layers, projected on the Ni–Ni and Ni–Al direction, as discussed in the main text for a bilayer structure with the average Q = 0.078 Å—similar to the Q of the experimental bulk low T structure.

The structural disproportionation of the bilayer octahedra is inhomogeneous: The in-plane NiO_6 bonds show disproportionation of about the same amplitude we would expect in the bulk. The interfacial bonds are less disproportionated; as the driving force on the apical oxygen atom comes only from the Ni, the disproportionation is lower. We can then estimate the relative stiffness of the Al–O bond relative to the Ni–O bonds from the relative displacements in a simple elastic spring model, to ∼86% of the stiffness of the Ni–O bonds. However, the additional energy cost per octahedron due to propagation in the NAO (or, equivalently, that NAO favors a state with no bond disproportionation) leads to a higher effective stiffness per octahedron. Finally, the out-of-plane bonds between nickelate layers in the bilayer structure disproportionate even more than the in-plane bonds, likely to compensate for the decreased interfacial disproportionation. The analysis is almost identical for the monolayer, with the exception of the nickelate interlayer out-of-plane bonds which do not exist.

The structural disproportionation Q leads to an on-site potential difference between the inequivalent Ni sites. As the oxygen atoms are closer to one Ni atom than the other, this leads to a difference in electrostatic potential. Within the context of our extended e_g Wannier orbitals, this can be read from the resulting Wannier Hamiltonian as the difference between the average on-site energy between the 2 inequivalent Ni sites:

$$\Delta_S = \bar{\epsilon}_{LF} - \bar{\epsilon}_{HF}, \quad [4]$$

where $\bar{\epsilon}_{LF}$ is the average on-site energy of the e_g orbitals on the Ni with a lower-filling and $\bar{\epsilon}_{HF}$ the average for the higher-filling octahedron. By analyzing multiple structures with varying amounts of structural disproportionation Q, we find that the difference in on-site potential Δ_S is linear in Q and takes the form $\Delta_S = gQ$, with g a parameter we can determine, in agreement with previous work (8). From interpolating Δ_S vs. Q within DFT from multiple structures with varying Q, we can obtain a bare coupling g^{DFT}. As the on-site electrostatic potential difference Δ_S has to be adjusted for double counting when performing a DMFT calculation (8, 32) (part of the on-site potential comes from Hartree interactions that appear both in DFT and DMFT), the coupling has to be adjusted within DFT+DMFT as well: $g = g^{DFT}(1 + (U - \frac{5}{3}J)\chi_0)$. The value of g^{DFT} is relatively constant between the bulk and heterostructured materials and has been shown to be constant throughout the $RNiO_3$ family, with $\chi_0 = \frac{\partial \Delta N}{\partial \Delta_S}$ the electronic susceptibility as extracted from DFT. However, as χ_0 is related to the inverse of the bandwidth (the occupancy changes more for the same on-site shift if the bands are narrower), the g across the materials changes slightly depending on the choice of U, J.

Electronic Structure

The dominant effect of the layering in the case of the heterostructures is electronic confinement: Electron hopping is confined to be in-plane only for the NNO monolayer and confined between the 2 layers for the bilayer. While the bulk orbitals have a bandwidth of 2.6 eV, the $3z^2 - r^2$ orbital for the monolayer has a bandwidth of 1.85 eV and for the bilayer 2.15 eV. Two other, more minor effects appear as well. Similar to previous work (40), the bond angles from the NAO propagate into the NNO, leading to straighter in-plane bond angles and slightly higher in-plane bandwidths in the heterostructures than for bulk NNO. This leads to a $x^2 - y^2$ bandwidth of 2.72 eV for the monolayer and 2.68 eV for the bilayer. Previous work has shown that one can use the bond angles of the counterlayers as a control parameter to tune the MIT temperature in nickelate heterostructures (40–42).

For a lower number of layers as in this work, however, the electronic confinement dominates and leads to an increased tendency to disproportionate. A third effect of heterostructuring on the electronic structure is that of the crystal-field splitting induced by the inequivalence of the bonds and the relative ionicity of the material. Finally, within the e_g Wannier picture, the monolayer also shows a crystal-field splitting of $\bar{\epsilon}_{x^2-y^2} - \bar{\epsilon}_{3z^2-r^2} = 0.14eV$ in DFT. We've performed calculations for the monolayer with the crystal-field splitting set to 0 for $U = 2.1$ eV and found that the critical J for the spontaneous ($Q = 0$) MIT transition line is the same as with the crystal-field splitting set to the DFT relaxed value, within an accuracy of $J = 0.01$ eV, thus showing a negligible effect (*SI Appendix*).

The simplest way to quantify the effect of the change in bandwidth is by comparing the static electronic response to an on-site field in our e_g tight-binding model, χ_0 as defined previously. By reading off ΔN vs. Δ_S from multiple structures with varying amounts of structural disproportionation, we obtain: $\chi_0^{bulk} = 1.16/eV$, $\chi_0^{bilayer} = 1.25/eV$, and $\chi_0^{monolayer} = 1.39/eV$.

The result of electronic confinement can be clearly seen in Fig. 4 in the curves showing ΔN as a function of Q. As a response to the same structural disproportionation Q, for the same U, J parameters, the monolayer is always more electronically disproportionated than the bilayer, which is always more electronically disproportionated than the bulk material ($\Delta N_{monolayer} > \Delta N_{bilayer} > \Delta N_{bulk}$). Further, there is a range of U, J parameters (Fig. 4, *Middle*) for which the heterostructures can be insulating, even in the absence of any structural disproportionation ($Q = 0$).

We have then found 3 main effects of heterostructuring on the electronic structure. The effect of layer confinement strongly lowers the kinetic energy of the electrons and favors an insulating state, with its effect primarily on the $3z^2 - r^2$ orbital. The bond-angle propagation leads to a small effect in the opposite direction, primarily on the $x^2 - y^2$ band. Finally, the crystal-field splitting is only significant in the monolayer; however, it does not affect the electronic transition.

Equilibrium Bond and Electronic Disproportionation from Total Energy Model

We now turn to determining equilibrium points in the energy functional from Eq. **1**. Stationarity of ΔE with respect to variations in ΔN and Q implies the 2 equilibrium conditions:

$$0 = kQ - \frac{1}{2}g\Delta N, \quad [5]$$

and:

$$0 = -\frac{1}{2}gQ + \frac{\partial E_{el}(\Delta N)}{\partial \Delta N}. \quad [6]$$

Eq. **5** gives Q as a function of ΔN However, its meaning is very simple: For a particular value of the electronic disproportionation ΔN, one can obtain the equilibrium structural displacement Q of the oxygen atoms as a result of the resulting electrostatic forces. Eq. **6** gives ΔN as a function of Q, as obtained via the DFT+DMFT method.

Combining the 2, we have an equation of state (8):

$$\frac{2k}{g}Q = \Delta N[Q]. \quad [7]$$

In practical terms, we can use this equation in a very simple manner: Using the stiffness k and coupling g obtained from the interpolation from DFT calculations and adjusting g for double counting, we can obtain the equilibrium Q for a particular ΔN as $Q = g\Delta N/2k$. Separately, we obtain the equilibrium ΔN as a function of Q from explicitly DFT+DMFT calculations rather than from Eq. **7**. The effect of Q is simulated by applying on-site terms to the $Q = 0$ Hamiltonian, namely, $\Delta_S/2$ to

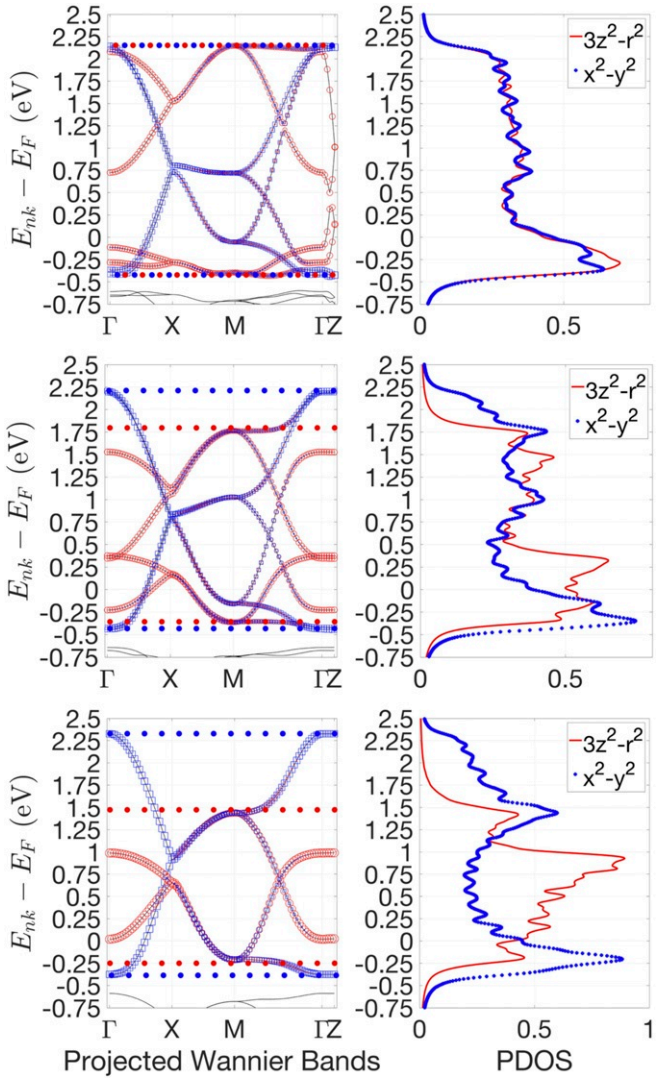

Fig. 3. Projected density of states of low-energy e_g Wannier bands for generalized gradient approximation-relaxed structures for bulk (*Top*), bilayer (*Middle*), and monolayer (*Bottom*) structures. Dotted horizontal lines show the approximate cutoff for determining bandwidths mentioned in the main text. Confinement greatly reduces the bandwidth of the $3z^2 - r^2$ orbital; however, the bond-angle propagation leads to a slightly wider bandwidth of the $x^2 - y^2$ orbital.

simulate the short-bond octahedron and $-\Delta_S/2$ the long-bond octahedron, where Δ_S is obtained from Q simply by multiplying $\Delta_S = gQ$. Single-shot DMFT calculations are then performed on the resulting Hamiltonian to obtain ΔN. The intersection of the functions $\Delta N[Q]$ and $Q[\Delta N]$ then determine equilibrium solutions for the material.

The $\Delta N(Q)$ relation is shown in Fig. 4 as large symbols connected by lines for $U = 2.1eV$ and 3 J values. For the smallest J value, neither the bulk nor the superlattice materials show a spontaneous disproportionation at $Q = 0$; for small Q, there is a regime in which the disproportionation is linear in Q, and the solution remains metallic. Above a particular Q, there is a very rapid cross-over to an insulating solution with a ΔN which is large and only weakly dependent on Q. In the insulating regime, the monolayer has a larger disproportionation than the bulk, with the bilayer in between. For an intermediate J, the monolayer and bilayer exhibit a spontaneous disproportionation at $Q = 0$, but the bulk material exhibits a Q-driven first-order transition. At the larger J, all 3 systems spontaneously distort at $Q = 0$.

Also shown in Fig. 4 are straight lines corresponding to the $Q(\Delta N)$ relation from Eq. **5**. The intersection of these lines with the DMFT $\Delta N(Q)$ curves defines the actual values of ΔN and Q. We see from the relative positions of the intersections that $Q_{monolayer} < Q_{bilayer} < Q_{bulk}$ and $\Delta N_{monolayer} > \Delta N_{bilayer} > \Delta N_{bulk}$. From an electronic point of view, the monolayer and bilayer are more disproportionated (ΔN is larger), as ΔN does not depend strongly on Q; however, the higher stiffness of the heterostructures leads to a lower Q. Further, as shown in Fig. 4, *Middle*, there is a range of U, J for which the heterostructures will stay insulating, even at a very small Q, while the bulk becomes metallic.

The relative roles of the lattice and electronic structure are easily disentangled from the above. First, the electronic disproportionation has a first-order transition, followed by a very slowly varying ΔN in the insulating phase. Assuming that ΔN is nearly constant in the insulating phase $\Delta N \approx N_{insulating}$, Q is then set by

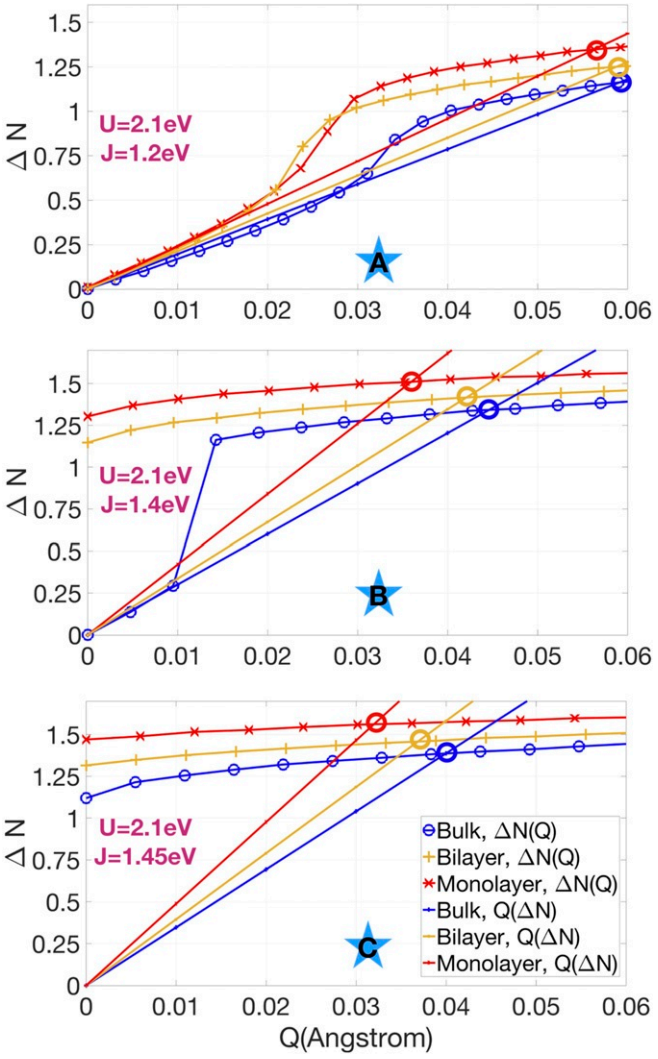

Fig. 4. ΔN vs. bond disproportionation Q within DFT+DMFT for bulk, bilayer, and monolayer structures, as well as Q vs. ΔN lines from the total energy model calculation in different areas of the phase space, as determined by Eqs. **5** and **6** via DFT+DMFT, as described in the main text. The thick circles mark the intersections that respect the equation of state 7. The panels marked with A, B, and C correspond to the points marked with stars in the phase diagram in *SI Appendix*, Fig. S1.

optimizing the structure $Q[\Delta N]$ in Eq. **4** as approximately $Q \approx \frac{g\Delta N_{insulating}}{2k}$. This allows the seemingly paradoxical solutions with the amplitude of Q and ΔN showing opposite trends between the bulk and heterostructure. If we assume that the experimentally obtained MIT temperature is more strongly correlated to ΔN than Q, while the X-ray absorption spectroscopy (XAS) spectra splitting is more strongly correlated with Q, we can thus explain the seemingly paradoxical results in previous work (9).

One of the signatures associated with the bond-disproportionated phase of the RNO nickelates is an increased peak–prepeak splitting of the XAS Ni L_3 edge, which in the monolayer and bilayer were found to be in between the values of the bulk disproportionated and undisproportionated structures throughout the insulating temperature range scanned. Consistent with this result, we find that the predicted value of the structural disproportionation of the monolayer is lower than the bulk, with the bilayer in between the 2. Further, XAS integration of the monolayer in-plane and out-of-plane Ni L_3 edge has found an orbital polarization of 8%, favoring the $3z^2 - r^2$ orbital. Within our insulating solutions, we find that orbital polarization is strongly suppressed ($<2\%$); however, we consistently find that the long-bond site has an orbital polarization of 5–8% in a direction consistent with experiment, while the LB site is orbitally polarized of about the same magnitude, but in the opposite direction. This suggests that the XAS spectra may sample primarily the LB; however, further theoretical and experimental work is needed.

Conclusion and Outlook

Using a combination of DFT+DMFT and many-body theory, we have elucidated the relative importance of lattice and electronic effects in heterostructured materials. We have found that the higher lattice energy cost in the heterostructured materials decreases the structural signatures of the symmetry-broken phase within the correlated material going through an MIT but that the distortion associated with it can propagate into the epitaxial layer. We have found that, as the effect of interactions is increased in a layer-confined structure, electronic disproportionation can be higher despite lower structural distortions in a heterostructure. Through comparison with experiment (9), our study suggests that the electronic disproportionation is more likely to be correlated to the MIT temperature than the structural disproportionation, which is suppressed by the higher structural stiffness of the material. At the same time, our work suggests that the structural disproportionation is more strongly connected to the XAS splitting observed experimentally, likely via the induced on-site electrostatic potential difference.

These general results can be used both to understand other similar heterostructures (for example, $LaNiO_3/LaAlO_3$) as well as to design new materials. Our analysis of the bond-disproportionation mode on the interfacial structure in this class of materials as well as in related classes of materials (vanadates, manganites, etc.) can be studied both theoretically and experimentally. The combination of bond angles, confinement, and relative structural stiffness can be used to fine-tune MIT temperatures. Based on the methodology in this work and previous work (3, 8), future work involving DFT+DMFT, DFT+U studies, and model calculations can address the relative roles of lattice and electronic disproportionation.

Methods

For our calculations, we use structures obtained from fully relaxed DFT+U calculations (43) and impose 0% strain relative to the theoretical DFT bulk NNO lattice constant on the heterostructures. We use Quantum Espresso, ultrasoft pseudopotentials, either from the GBRV or generated by using the Vanderbilt ultrasoft pseudopotential generator as described (43–47) and benchmark our results against experimental bulk structures. The disproportionated structures have 2 inequivalent Ni sites, 1 with relatively long Ni–O bonds (LB) and 1 with relatively short Ni–O bonds (SB). We define the structural order Q as:

$$Q = \sqrt{\frac{\sum_i \left(l_{LB}^{(i)} - l_{SB}^{(i)}\right)^2}{6}}, \quad [8]$$

where $l^{(i)}$ are the lengths of the Ni–O bonds.

For each structure, we then perform a self-consistent DFT calculation and fit the bands arising from the frontier e_g orbitals using maximally localized Wannier functions as implemented in Wannier90 (48, 49). Bands for representative structures near the Fermi level and their Wannier fits are shown in Fig. 3. The parameter g in Eq. **5** is defined in terms of the on-site energy difference $\Delta_S = gQ$ entering our DMFT calculations. In our 1 shot DMFT, g is corrected from the DFT value by a double-counting term (8, 32), so $g = g^{DFT}(1 + (U - \frac{5}{3}J)\chi_0)$.

The Wannier fits define a low-energy tight-binding model to which we add standard Slater–Kanamori interactions and solve using DMFT [using the TRIQS library (50), ct-hyb solver (51), and dfttools (52) interface] with the 2 inequivalent Ni treated as different embedded atoms.

The parameter k is the stiffness to lattice distortions at fixed ΔN. We argue, following refs. 3 and 8, that since the stiffness comes from the full electronic structure at fixed ΔN, the frontier orbitals play a relatively minor role and, for the purpose of calculating k, may be treated at the DFT level. We therefore obtain k from the dependence of the DFT energy on Q $\frac{\partial E_{DFT}}{\partial Q} = cQ$. However, in the DFT calculations, ΔN is relaxed at each Q. Referring to Eq. **5**, we have on the DFT level (and noting the stationarity with respect to ΔN):

$$cQ = \frac{\partial E_{DFT}}{\partial Q} = kQ - \frac{1}{2} g^{DFT} \Delta N^{DFT}(Q). \quad [9]$$

In the linear response regime, which accurately describes the DFT results for all structures we considered, we find:

$$\frac{cQ^2}{2} = E_{DFT}(Q) = \left(\frac{k}{2} - \frac{1}{4}\left(g^{DFT}\right)^2 \chi_0\right) Q^2. \quad [10]$$

We can then extract c from the energy of continuously varying structures with different Q. Combining this with knowledge of g^{DFT} and χ_0 as described below, we can then obtain the stiffness k. The parameter g^{DFT} is defined in terms of the average on-site energy Δ_S^{DFT} obtained from our Wannier fits to DFT band structures, as $g^{DFT} = \frac{\Delta_S^{DFT}}{Q}$ and $\Delta N(Q)$ is obtained from the occupancy difference of the Wannier orbitals and is found to be linear in Q, $\Delta N = \chi_0 g^{DFT} Q$. This relation defines the on-site susceptibility χ_0. g^{DFT} can be read off from the on-site energy difference and is nearly identical for all 3 materials, namely, 2.89 eV/Å for bulk, 2.972 eV/Å for the bilayer, and 2.962 eV/Å for the monolayer. This means that a similar movement of the ions leads to a similar change of electrostatic potential, which is something we would expect as the local environment is similar.

ACKNOWLEDGMENTS. We thank Sohrab Ismail-Beigi, Jean-Marc Triscone, Hugo U. R. Strand, Manuel Zingl, Alexander Hampel, and Claude Ederer for helpful conversations; and Nick Carriero and the Scientific Computing Core division of the Flatiron Institute for invaluable technical assistance. The Flatiron Institute is a division of the Simons Foundation. A.G. was supported by European Research Council Grant ERC-319286-QMAC. O.E.P. was supported by Forschungsförderungsgesellschaft Competence Centers for Excellent Technologies Program IC-MPPE (Project 859480).

1. H. Park, A. J. Millis, C. Marianetti, Total energy calculations using DFT+DMFT: Computing the pressure phase diagram of the rare earth nickelates. *Phys. Rev. B* **89**, 245133 (2014).
2. H. Park, A. J. Millis, C. A. Marianetti, Computing total energies in complex materials using charge self-consistent DFT+DMFT. *Phys. Rev. B Condens. Matter Mater Phys.* **90**, 1–17 (2014).
3. Q. Han, A. Millis, Lattice energetics and correlation-driven metal-insulator transitions: The case of Ca_2RuO_4. *Phys. Rev. Lett.* **121** 67601 (2018).
4. K. Haule, G. L. Pascut, Forces for structural optimizations in correlated materials within a DFT+embedded DMFT functional approach. *Phys. Rev. B* **94**, 1–16 (2016).
5. K. Haule, G. L. Pascut, Mott transition and magnetism in rare earth nickelates and its fingerprint on the x-ray scattering. *Nat. Sci. Rep.* **7**, 10375 (2017).
6. S. Mandal, P. Zhang, S. Ismail-Beigi, K. Haule, How correlated is the FeSe/$SrTiO_3$ system?*Phys. Rev. Lett.* **119**, 1–6 (2017).
7. B. A. Amadon, A self-consistent DFT+DMFT scheme in the projector augmented wave method: Applications to cerium, $Ce2O_3$ and $Pu2O_3$ with the Hubbard I solver and comparison to DFT+U. *J. Phys. Condens. Matter* **24**, 075604 (2012).

8. O. E. Peil, A. Hampel, C. Ederer, A. Georges, Mechanism and control parameters of the coupled structural and metal-insulator transition in nickelates. *Phys. Rev. B* **99**, 245127 (2019).
9. A. S. Disa *et al.*, Control of hidden ground-state order in $NdNiO_3$ superlattices. *Phys. Rev. Mater.* **1**, 024410 (2017).
10. S. Catalano *et al.*, Rare-earth nickelates $RNiO_3$: Thin films and heterostructures. *Rep. Prog. Phys.* **81**, 046501 (2018).
11. S. Ismail-Beigi, F. J. Walker, A. S. Disa, K. M. Rabe, C. H. Ahn, Picoscale materials engineering, *Nat. Rev. Mat.* **2**, 17060 (2017).
12. A. V. Boris *et al.*, Dimensionality control of electronic phase transitions in nickel-oxide superlattices. *Sci. Rep.* **332**, 937–940 (2011).
13. D. P. Kumah *et al.*, Tuning the structure of nickelates to achieve two-dimensional electron conduction. *Adv. Mater.* **26**, 1935–1940 (2014).
14. S. Middey *et al.*, Disentangled cooperative orderings in artificial rare-earth nickelates. *Phys. Rev. Lett.* **120**, 156801(2018).
15. A. X. Gray *et al.*, Insulating state of ultrathin epitaxial $LaNiO_3$ thin films detected by hard X-ray photoemission. *Phys. Rev. B. Condens. Matter Mater Phys.* **84**, 1–6 (2011).
16. S. Stemmer, A. J. Millis. Quantum confinement in oxide quantum wells. *MRS Bull.* **38**, 1032–1039 (2013).
17. P. J. Phillips *et al.*, Experimental verification of orbital engineering at the atomic scale: Charge transfer and symmetry breaking in nickelate heterostructures. *Phys. Rev. B.* **95**, 205131 (2017).
18. J. Y. Zhang, H. Kim, E. Mikheev, A. J. Hauser, S. Stemmer, Key role of lattice symmetry in the metal-insulator transition of $NdNiO_3$ films. *Sci. Rep.* **6**, 23652 (2016).
19. J. Shamblin *et al.*, Experimental evidence for bipolaron condensation as a mechanism for the metal-insulator transition in rare-earth nickelates. *Nat. Commun.* **9**, 86 (2018).
20. D. Meyers *et al.*, Pure electronic metal-insulator transition at the interface of complex oxides. *Sci. Rep.* **6**, 27934 (2016).
21. M. Först *et al.*, Multiple supersonic phase fronts launched at a complex-oxide heterointerface. *Phys. Rev. Lett.* **118**, 027401 (2017).
22. M. Forst *et al.*, Spatially resolved ultrafast magnetic dynamics initiated at a complex oxide heterointerface. *Nat. Mater.* **14**, 883–888 (2015).
23. M. Medarde, P. Lacorre, K. Conder, F. Fauth, A. Furrer, Giant ^{16}O-^{18}i isotope effect on the metal-insulator transition of $RNiO_3$ perovskites (R = rare earth). *Phys. Rev. Lett.* **80**, 2397–2400 (1998).
24. W. Hu, S. Catalano, M. Gibert, J. M. Triscone, A. Cavalleri, Broadband terahertz spectroscopy of the insulator-metal transition driven by coherent lattice deformation at the $SmNiO_3/LaAlO_3$ interface. *Phys. Rev. B* **93**, 161107(R) (2016).
25. A. D. Caviglia *et al.*, Photoinduced melting of magnetic order in the correlated electron insulator $NdNiO_3$. *Phys. Rev. B Condens. Matter Mater. Phys.* **88**, 220401(R) (2013).
26. G. G. Guzman-Verri, R. T. Brierley, P. B. Littlewood, Elastic interactions and control of the Mott transition. arXiv:1701.02318 (9 January 2017).
27. B. Mandal *et al.*, The driving force for charge ordering in rare earth nickelates. arXiv:1701.06819 (24 January 2017).
28. H. Park, A. J. Millis, C. A. Marianetti, Influence of quantum confinement and strain on orbital polarization of four-layer $LaNiO_3$ superlattices: A DFT+DMFT study. *Phys. Rev. B* **93**, 1–10 (2016).
29. J. Ruppen *et al.*, Optical spectroscopy and the nature of the insulating state of rare-earth nickelates. *Phys. Rev. B Condens. Matter Mater. Phys.* **92**, 155145 (2015).
30. O. E. Peil, M. Ferrero, A. Georges, Orbital polarization in strained $LaNiO_3$: Structural distortions and correlation effects. *Phys. Rev. B Condens. Matter Mater. Phys.* **90**, 045128 (2014).
31. M. J. Han, X. Wang, C. A. Marianetti, A. J. Millis, Dynamical mean-field theory of nickelate superlattices. *Phys. Rev. Lett.* **107**, 206804 (2011).
32. P. Seth *et al.*, Renormalization of effective interactions in a negative charge transfer insulator. *Phys. Rev. B* **96**, 205139 (2017).
33. A. Subedi, O. E. Peil, A. Georges, Low-energy description of the metal-insulator transition in the rare-earth nickelates. *Phys. Rev. B Condens. Matter Mater. Phys.* **91**, 1–16 (2015).
34. H. U. R. Strand, Valence-skipping and negative-U in the d-band from repulsive local Coulomb interaction. *Phys. Rev. B Condens. Matter Mater. Phys.* **90**, 155108 (2014).
35. A. Blanca-Romero, R. Pentcheva, Confinement-induced metal-to-insulator transition in strained $LaNiO_3/LaAlO_3$ superlattices. *Phys. Rev. B Condens. Matter Mater. Phys.* **84**, 195450 (2011).
36. O. Janson, K. Held, Finite-temperature phase diagram of (111) nickelate bilayers. *Phys. Rev. B* **98**, 115118 (2018).
37. H. Park, A. J. Millis, C. A. Marianetti, Site-selective Mott transition in rare-earth-element nickelates. *Phys. Rev. Lett.* **109**, 156402 (2012).
38. A. Mercy, J. Bieder, J. Iniguez, P. Ghosez, Structurally triggered metal-insulator transition in rare-earth nickelates. *Nat. Commun.* **8**:1677 (2017).
39. S. Johnston, A. Mukherjee, I. Elfimov, M. Berciu, G. A. Sawatzky, Charge disproportionation without charge transfer in the rare-earth-element nickelates as a possible mechanism for the metal-insulator transition. *Phys. Rev. Lett.* **112**, 106404 (2014).
40. Z. Liao *et al.*, Metal-insulator-transition engineering by modulation tilt-control in perovskite nickelates for room temperature optical switching. *Proc. Natl. Acad. Sci. U.S.A.* **115**, 9515–9520 (2018).
41. S. H. Chang *et al.*, Thickness-dependent structural phase transition of strained $SrRuO_3$ ultrathin films: The role of octahedral tilt. *Phys. Rev. B Condens. Matter Mater. Phys.* **84**, 104101 (2011).
42. R. Gao *et al.*, Interfacial octahedral rotation mismatch control of the symmetry and properties of $SrRuO_3$. *ACS Appl. Mater. Inter.* **8**, 14871–14878 (2016).
43. V. I. Anisimov, F. Aryasetiawan, A. Liechtenstein. First-principles calculations of the electronic structure and spectra of strongly correlated systems: The LDA+*U* method. *J. Phys. Condens. Matter* **9**, 767–808 (1997).
44. P. Giannozzi *et al.*, Quantum ESPRESSO: A modular and open-source software project for quantum simulations of materials. *J. Phys. Condens. Matter* **21**, 395502 (2009).
45. D. Vanderbilt, Soft self-consistent pseudopotentials in a generalized eigenvalue formalism. *Phys. Rev. B* **41**, 7892–7895, 1990.
46. K. F. Garrity, J. W. Bennett, K. M. Rabe, D. Vanderbilt, Pseudopotentials for high-throughput DFT calculations. *Comput. Mater. Sci.* **81**, 446–452 (2014).
47. H. Chen *et al.*, Reversible modulation of orbital occupations via an interface- induced polar state in metallic manganites. *Nano. Lett.* **14**, 4965–4970 (2014).
48. A. A. Mostofi *et al.*, An updated version of wannier90: A tool for obtaining maximally-localised Wannier functions. *Comput. Phys. Commun.* **185**, 2309–2310 (2014).
49. N. Marzari, A. A. Mostofi, J. R. Yates, I. Souza, D. Vanderbilt, Maximally localized Wannier functions: Theory and applications. *Rev. Mod. Phys.* **84**, 1419–1475 (2012).
50. O. Parcollet *et al.*, Triqs: A toolbox for research on interacting quantum systems. *Comput. Phys Commun*, **196** 398–415 (2015).
51. P. Seth, I. Krivenko, M. Ferrero, O. Parcollet, TRIQS/CTHYB: A continuous-time quantum Monte Carlo hybridisation expansion solver for quantum impurity problems. *Comput. Phys. Commun.* **200**, 274–284 (2016).
52. M. Aichhorn *et al.*, TRIQS/DFTTools: A TRIQS application for ab initio calculations of correlated materials. *Comput. Phys. Commun.* **204**, 200–208 (2016).